

## Detection of low energy antiproton annihilations in a segmented silicon detector

---

S. Aghion<sup>a,b</sup>, O. Ahlén<sup>c</sup>, A. S. Belov<sup>d</sup>, G. Bonomi<sup>e,f</sup>, P. Bräunig<sup>g</sup>, J. Bremer<sup>c</sup>, R. S. Brusa<sup>h</sup>, G. Burghart<sup>c</sup>, L. Cabaret<sup>i</sup>, M. Caccia<sup>j</sup>, C. Canali<sup>k</sup>, R. Caravita<sup>l</sup>, F. Castelli<sup>l</sup>, G. Cerchiari<sup>m</sup>, S. Cialdi<sup>l</sup>, D. Comparat<sup>i</sup>, G. Consolati<sup>a,b</sup>, J.H. Derking<sup>c</sup>, S. Di Domizio<sup>n</sup>, L. Di Noto<sup>h</sup>, M. Doser<sup>c</sup>, A. Dudarev<sup>c</sup>, R. Ferragut<sup>a,b</sup>, A. Fontana<sup>f</sup>, P. Genova<sup>f</sup>, M. Giammarchi<sup>b</sup>, A. Gligorova<sup>o\*</sup>, S. N. Gninenko<sup>d</sup>, S. Haider<sup>c</sup>, J. Harasimowicz<sup>p</sup>, T. Huse<sup>q</sup>, E. Jordan<sup>m</sup>, L. V. Jørgensen<sup>c</sup>, T. Kaltenbacher<sup>c</sup>, A. Kellerbauer<sup>m</sup>, A. Knecht<sup>c</sup>, D. Krasnický<sup>r</sup>, V. Lagomarsino<sup>r</sup>, A. Magnani<sup>f,s</sup>, S. Mariazzi<sup>t</sup>, V. A. Matveev<sup>d,u</sup>, F. Moia<sup>a,b</sup>, G. Nebbia<sup>v</sup>, P. Nédélec<sup>w</sup>, N. Pacifico<sup>o</sup>, V. Petráček<sup>x</sup>, F. Prelz<sup>b</sup>, M. Prevedelli<sup>y</sup>, C. Regenfus<sup>k</sup>, C. Riccardi<sup>s,f</sup>, O. Røhne<sup>q</sup>, A. Rotondi<sup>s,f</sup>, H. Sandaker<sup>o</sup>, A. Sosa<sup>p</sup>, M. A. Subieta Vasquez<sup>e,f</sup>, M. Špaček<sup>x</sup>, G. Testera<sup>n</sup>, C. P. Welsch<sup>p</sup> and S. Zavatarelli<sup>n</sup>,

(AEgIS collaboration)

- <sup>a</sup>Politecnico di Milano, Piazza Leonardo da Vinci 32, 20133 Milano, Italy
- <sup>b</sup>Istituto Nazionale di Fisica Nucleare, Sez. di Milano, Via Celoria 16, 20133 Milano, Italy
- <sup>c</sup>European Organisation for Nuclear Research, Physics Department, 1211 Geneva 23, Switzerland
- <sup>d</sup>Institute for Nuclear Research of the Russian Academy of Sciences, Moscow 117312, Russia
- <sup>e</sup>University of Brescia, Department of Mechanical and Industrial Engineering, Via Branze 38, 25133 Brescia, Italy
- <sup>f</sup>Istituto Nazionale di Fisica Nucleare, Sez. di Pavia, Via Agostino Bassi 6, 27100 Pavia, Italy
- <sup>g</sup>University of Heidelberg, Kirchhoff Institute for Physics, Im Neuenheimer Feld 227, 69120 Heidelberg, Germany
- <sup>h</sup>Department of Physics, University of Trento and TIFPA-INFN, Via Sommarive 14, 38123 Povo, Trento, Italy
- <sup>i</sup>Laboratoire Aimé Cotton, CNRS, Université Paris Sud, ENS Cachan, Bâtiment 505, Campus d'Orsay, 91405 Orsay Cedex, France
- <sup>j</sup>Insubria University, Como-Varese, Italy
- <sup>k</sup>University of Zurich, Physics Institute, Winterthurerstrasse 190, 8057 Zurich, Switzerland
- <sup>l</sup>University of Milano, Department of Physics, Via Celoria 16, 20133 Milano, Italy
- <sup>m</sup>Max Planck Institute for Nuclear Physics, Saupfercheckweg 1, 69117 Heidelberg, Germany
- <sup>n</sup>Istituto Nazionale di Fisica Nucleare, Sez. di Genova, Via Dodecaneso 33, 16146 Genova, Italy
- <sup>o</sup>University of Bergen, Institute of Physics and Technology, Allégaten 55, 5007 Bergen, Norway
- <sup>p</sup>University of Liverpool and the Cockcroft Institute, Liverpool, Sci-Tech Daresbury, Keckwick Lane, Daresbury, Warrington, WA4 4AD, United Kingdom
- <sup>q</sup>University of Oslo, Department of Physics, Sem Sælandsvei 24, 0371 Oslo, Norway
- <sup>r</sup>University of Genoa, Department of Physics, Via Dodecaneso 33, 16146 Genova, Italy
- <sup>s</sup>University of Pavia, Department of Nuclear and Theoretical Physics, Via Bassi 6, 27100 Pavia, Italy
- <sup>t</sup>Stefan Meyer Institute for subatomic Physics, Boltzmanngasse 3, 1090 Vienna, Austria
- <sup>u</sup>Joint Institute for Nuclear Research, 141980 Dubna, Russia
- <sup>v</sup>Istituto Nazionale di Fisica Nucleare, Sez. di Padova, Via Marzolo 8, 35131 Padova, Italy
- <sup>w</sup>Claude Bernard University Lyon 1, Institut de Physique Nucléaire de Lyon, 4 Rue Enrico Fermi, 69622 Villeurbanne, France
- <sup>x</sup>Czech Technical University in Prague, FNSPE, Břehová 7, 11519 Praha 1, Czech Republic
- <sup>y</sup>University of Bologna, Department of Physics, Via Irnerio 46, 40126 Bologna, Italy

*E-mail:* Angela.Gligorova@cern.ch

ABSTRACT: The goal of the AEGIS experiment at the Antiproton Decelerator (AD) at CERN, is to measure directly the Earth's gravitational acceleration on antimatter by measuring the free fall of a pulsed, cold antihydrogen beam. The final position of the falling antihydrogen will be detected by a position sensitive detector. This detector will consist of an active silicon part, where the annihilations take place, followed by an emulsion part. Together, they allow to achieve 1% precision on the measurement of  $\bar{g}$  with about 600 reconstructed and time tagged annihilations. We present here the prospects for the development of the AEGIS silicon position sensitive detector and the results from the first beam tests on a monolithic silicon pixel sensor, along with a comparison to Monte Carlo simulations.

KEYWORDS: AEGIS, silicon, monolithic planar pixel, antiproton, annihilation, GEANT4, antihydrogen.

---

\*Corresponding author.

---

## Contents

<b>1. Introduction</b>	<b>2</b>
<b>2. Development of the silicon detector for AEGIS</b>	<b>3</b>
2.1 Annihilation of antiprotons in silicon	3
2.2 Monte Carlo simulations	3
2.3 Detector requirements and design	5
<b>3. Test beam setup</b>	<b>7</b>
3.1 Antiproton source and test facility	7
3.2 The MIMOTERA detector	8
3.3 Calibration of the MIMOTERA detector and clustering	9
<b>4. Results</b>	<b>11</b>
4.1 Data selection	11
4.2 Background sources	12
4.3 Cluster characteristics	15
4.4 Tracks recognition	16
4.5 Comparison with Monte Carlo simulations	17
<b>5. Summary and Conclusions</b>	<b>19</b>

---

# 1. Introduction

The AEGIS experiment [1] at CERN (fig. 1) aims at verifying the Weak Equivalence Principle for antimatter by measuring the Earth's gravitational acceleration  $g$  for antihydrogen. Several attempts have been made in the past to measure the gravitational constant for antimatter, both for charged [2, 3] and neutral antiparticles [4, 5, 6]. However, none of these experiments brought to conclusive results. Recently, a study from the ALPHA collaboration [7] sets limits to the ratio of gravitational mass to the inertial mass of antimatter but is yet far from testing the equivalence principle. Another experiment, GBAR, [8] has been proposed but not yet built.

Cold antihydrogen (100 mK) in Rydberg states will be produced through the charge exchange reaction between Rydberg positronium and cold antiprotons stored in a Penning trap [9]. Applying an appropriate electric field will accelerate the formed antihydrogen in a horizontal beam, with a typical axial velocity distribution spanning a few 100 m/s [10].

Some of the trajectories will be selected through a moiré deflectometer [11], which will consist of two vertical gratings producing a fringe pattern on a downstream annihilation plane (see fig. 2). This plane will be the first layer of the position sensitive detector where the antihydrogen will impinge with energies of the order of meV and annihilate. The vertical deflection of the pattern is proportional to the gravitational constant to be measured. Over a flight path of  $\sim 1$  m, the deflection is expected in the order of  $\sim 20 \mu\text{m}$  for a 1 g vertical acceleration [1]. A vertical resolution better than  $10 \mu\text{m}$  is required to meet the goal of 1% precision on the  $\bar{g}$  measurement with 600 reconstructed and time tagged annihilations [12].

According to the current design, the position sensitive detector will be a hybrid detector consisting of an active silicon part, where the annihilation takes place, followed by an emulsion part [12, 13]. The silicon detector will provide online measurement and diagnostics of the antiproton annihilations as well as the necessary time of flight information.

The aim of the present study is to perform the first measurement and direct detection of slow antiproton ( $\sim$  few 100 keV) annihilations in silicon. This is the first step towards understanding the signature of antihydrogen annihilations, which is one of the most fundamental aspects of designing

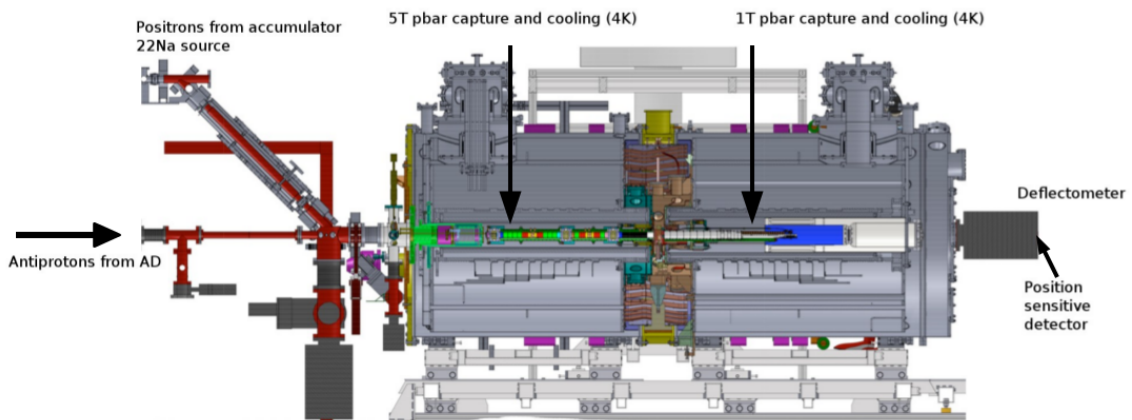


**Figure 1.** Schematic view of the central region of the AEGIS experiment.

28 a silicon position sensitive detector for AE $\bar{g}$ IS. To our knowledge, only in one other experiment  
29 annihilations in a silicon sensor were directly detected and simulated [14]. However, much faster  
30 antiprotons were used in that study (608 MeV/c) than in the study presented here.

## 31 **2. Development of the silicon detector for AE $\bar{g}$ IS**

32 In AE $\bar{g}$ IS, the silicon detector will act as the annihilation surface. Kinetic energy of the antihydro-  
33 gen atom will be insufficient to generate a detectable signal, so the antihydrogen will be indirectly  
34 detected through the detection of the annihilation products. We will now present available exper-  
35 imental data on the annihilation process of antihydrogen (antiprotons) in matter and the available  
36 Monte Carlo tools for its simulation. This constitutes the basis for the design of the AE $\bar{g}$ IS silicon  
37 detector, which will be presented in 2.3.

### 38 **2.1 Annihilation of antiprotons in silicon**

39 The annihilation process of antihydrogen in matter is similar to the one of an antiproton as the  
40 positron annihilates immediately when meeting an atomic electron. Previous experiments at LEAR  
41 [15] have studied annihilations of antiprotons in elements with different  $Z$ . In this process, the an-  
42 tiproton loses energy as it traverses matter and annihilates with a proton at rest creating charged  
43 ( $1.53 \pm 0.03$  per annihilation per charge sign) and neutral pions ( $1.96 \pm 0.23$  per annihilation). For  
44 elements with atomic numbers  $>1$  the average ratio is shifted towards producing more negatively  
45 charged pions, due to the possible annihilation of the antiproton with nuclear neutrons. The pions  
46 produced in the annihilation may further interact with other nucleons resulting in nuclear frag-  
47 ments and isolated neutrons and protons. For silicon, the stopping power of the lowest incoming  
48 antiproton energy so far measured (0.188 MeV) shows to be 32% lower than for protons [16].

49 Antimatter annihilation has been detected with silicon sensors previously [17], through the  
50 detection of pions emitted in the annihilation process. However, in our present application, for the  
51 first time the antiproton annihilates with a nucleon in the bulk of the detector itself. These pions are  
52 *Minimum Ionizing Particles* (MIPs) depositing  $\sim 0.3$  keV/ $\mu\text{m}$  [18] in matter, a negligible fraction  
53 compared with their average momentum of  $\sim 350$  MeV/c [19].

54 When the annihilation takes place on-sensor, the largest fraction of deposited energy is due  
55 to the heavy fragments. These fragments are *Highly Ionizing Particles* (or HIPs). Energy deposits  
56 and ranges in silicon for different annihilation products simulated using the SRIM [20] package are  
57 shown in fig. 3 and 4. HIPs (slow protons and heavier ions) deposit locally (within a few or tens of  
58  $\mu\text{m}$  from the interaction point) all of their kinetic energy. It becomes thus evident that being able  
59 to discriminate between the signal produced by HIPs or MIPs in the detector, can help increasing  
60 significantly the resolution on the annihilation position.

### 61 **2.2 Monte Carlo simulations**

62 In the present work we compare data with Monte Carlo simulations, using GEANT4, release  
63 4.9.5.p01, interfaced with VMC (Virtual Monte Carlo) software, release v2-13c [21]. Two par-  
64 ticular GEANT4 models were studied, CHIPS (QGSP BERT) and FTFP (FTFP BERT TRV).

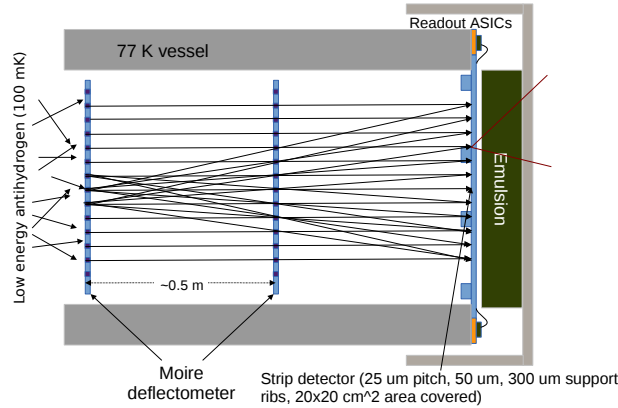


**Figure 2.** The moiré deflectometer producing a pattern on the position sensitive detector, where more particle paths intersect at the detector plane.

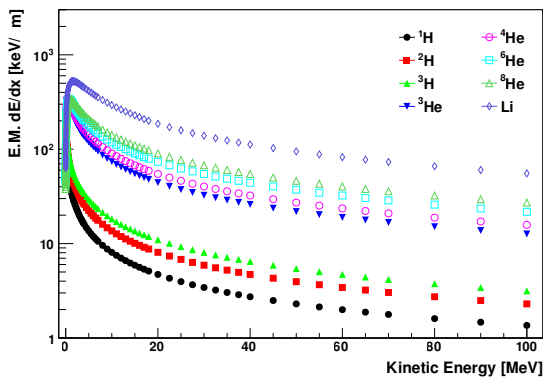


**Figure 3.** Energy deposition in silicon for different nuclear fragments that can be generated in an annihilation event, calculated with the SRIM package [20].

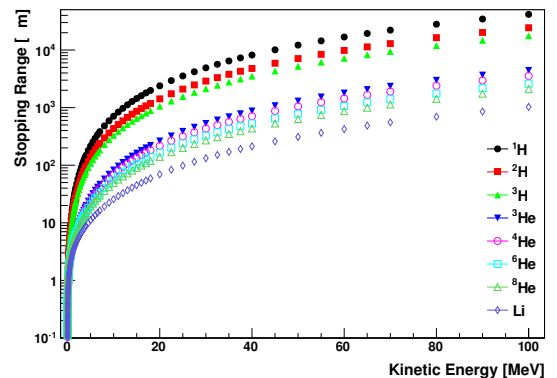


**Figure 4.** Stopping range in silicon for different nuclear fragments that can be generated in an annihilation event, calculated with the SRIM package.

65 The CHIPS (CHiral Invariant Phase Space) model [22] is a 3D quark-level event generator for  
 66 the fragmentation of excited hadronic systems into individual hadrons, whereas the FTFP model  
 67 [23] relies on a string model to describe the interactions between quarks.

68 The CHIPS and FTFP models differ in the production rate and in the composition of the  
 69 annihilation products. CHIPS produces heavy nuclear fragments in only 20 % of the events while  
 70 FTFP generates heavy fragments in all of them. In addition, CHIPS produces more than three times  
 71 as many protons, neutrons and alpha particles in each collision, as seen in fig. 5, which provides  
 72 the multiplicities for the different products for annihilations at rest.

73 Both models can simulate annihilation of antiprotons with nuclei, though comparison of sim-  
 74 ulations to data for low-energy antiprotons in silicon is missing. CHIPS simulations have been  
 75 previously compared with uranium and carbon data, while the newer FTFP still lacks comparison  
 76 to data for antiproton energies below 120 MeV [24].

77 Table 1 shows a comparison of experimental values obtained for  $^{12}\text{C}$  and  $^{40}\text{Ca}$ , the two el-

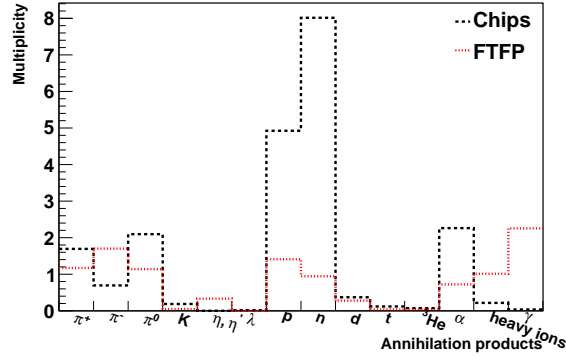


**Figure 5.** Multiplicity of different annihilation products (per annihilation) as predicted by the two models CHIPS and FTFP, over the whole kinetic energy spectrum.

78 ements closest to silicon, with LEAR [25], and the simulated values for the same elements and  
 79 silicon. However, the values presented are for higher energies ( $> 6$  MeV) than in this study. The  
 80 table shows that for the kinetic energy range of 6-18 MeV, FTFP describes the data obtained for  
 81 protons better than CHIPS. On the other hand, CHIPS describes better the experimental values for  
 82 ion species with higher atomic numbers and for higher energies.

### 83 2.3 Detector requirements and design

84 As already shown in fig. 2, the AEgIS silicon position sensitive detector will act as a separation  
 85 membrane between the ultra high vacuum of the antihydrogen formation and transport region and  
 86 the secondary vacuum where the emulsion planes will be positioned. The resulting design in-  
 87 cludes an array of co-planar single-sided silicon strip sensors, built with a strip pitch of  $25 \mu\text{m}$  and  
 88 mounted on a silicon mechanical support wafer, hosting the readout electronics. This system will  
 89 provide with the one-dimensional vertical ( $y$ ) deflection information, though an approach based on  
 90 resistive strips, able to provide the  $x$  coordinate as well, as demonstrated in [26], is currently under  
 91 study.

92 A further requirement of the silicon detector will be a thickness, in the active regions, of  $50$   
 93  $\mu\text{m}$ . This will allow to minimize the scattering of annihilation products, detected further down-  
 94 stream by the emulsion detector, allowing for a precise vertex reconstruction. To achieve the goal,  
 95 thick support ribs will guarantee the mechanical stability of the system, with size and position of  
 96 the ribs being optimized as to allow for the maximum efficiency of the detector in areas where a  
 97 higher beam luminosity is expected.

98 Finally, in order to avoid the black body radiation coming from the detector to increase the  
 99 antiproton plasma temperature (which would increase the thermal velocity of the antihydrogen),  
 100 the whole detector system will be kept at cryogenic temperatures ( $77$  K or lower). This will re-  
 101 quire the electronics to be designed for such conditions. The feasibility of operation of standard  
 102 CMOS readout ASICs in cryogenic temperatures has already been proven in [27]. The ASIC design  
 103 for AEgIS, under development, will rely on an improved integration and communication protocol



	Energy (MeV)	LEAR $^{12}\text{C}$	CHIPS $^{12}\text{C}$	FTFP $^{12}\text{C}$	LEAR $^{40}\text{Ca}$	CHIPS $^{40}\text{Ca}$	FTFP $^{40}\text{Ca}$	CHIPS $^{28}\text{Si}$	FTFP $^{28}\text{Si}$
p	6-18	$23.3 \pm 2.0$	$168.0 \pm 1.0$	$56.0 \pm 0.8$	$74.2 \pm 4.1$	$172.0 \pm 1.0$	$60.2 \pm 0.8$	$170.0 \pm 1.0$	$58.6 \pm 0.8$
d	8-24	$9.3 \pm 0.8$	$15.9 \pm 0.4$	$12.1 \pm 0.3$	$18.1 \pm 1.1$	$14.9 \pm 0.4$	$12.0 \pm 0.3$	$15.9 \pm 0.4$	$12.2 \pm 0.3$
t	11-29	$4.5 \pm 0.4$	$2.8 \pm 0.2$	$1.3 \pm 0.1$	$5.7 \pm 0.4$	$2.7 \pm 0.2$	$1.0 \pm 0.1$	$3.0 \pm 0.2$	$1.5 \pm 0.1$
$^3\text{He}$	36-70	$1.72 \pm 0.17$	$0.19 \pm 0.01$	$0.11 \pm 0.03$	$2.22 \pm 0.17$	$0.22 \pm 0.05$	$0.13 \pm 0.04$	$0.23 \pm 0.05$	$0.16 \pm 0.04$
$\alpha$	36-70	$1.14 \pm 0.12$	$1.8 \pm 0.1$	0	$2.18 \pm 0.16$	$1.9 \pm 0.1$	0	$1.8 \pm 0.1$	0

**Table 1.** Measured and simulated production yields (for 100 annihilations) for the most important nuclear fragments produced in annihilations of antiprotons with high  $A$  nuclei. Experimental data is from LEAR [25] for  $^{12}\text{C}$  and  $^{40}\text{Ca}$ , the two elements closest to silicon. *Energy* refers to the kinetic energy of the annihilations products. These measured values are compared with the simulated values for calcium, carbon and silicon using the two GEANT4 models, CHIPS and FTFP. FTFP describes the data obtained with protons better than CHIPS, while CHIPS seems to be a better description for ion species with higher atomic numbers and higher energies.

104 (enabling the readout of  $\sim 3000$  strips) and a wider dynamic range, to cope with the high energy  
105 deposited in the sensor from the annihilation events.

106 Given the complex nature of the annihilation process, Monte Carlo simulations will be required  
107 to validate reconstruction algorithms to be implemented in the final system. Part of the aim of the  
108 present work is the validation of the available simulation physics model, in the particular case  
109 of direct annihilation in a silicon sensor, with data available for the first time for low antiproton  
110 energies.

### 111 3. Test beam setup

#### 112 3.1 Antiproton source and test facility

113 The AEGIS experiment is situated at the Antiproton Decelerator (AD) which delivers  $\sim 3 \times 10^7$  low  
114 energy (5.3 MeV) and bunched ( $\sim 120$  ns) antiprotons every  $\sim 100$  s. During tests in May 2012  
115 the first section of the AEGIS experiment was in place, comprising a 5 T superconducting solenoid  
116 magnet enclosing a Penning trap in an ultrahigh vacuum (UHV) of  $10^{-11}$  mbar.

117 While passing through the AEGIS apparatus, the antiprotons lose energy first through two  
118 aluminum degraders, one fixed ( $18 \pm 2.7 \mu\text{m}$ ) and one mobile ( $0.8 \pm 0.2$ ,  $2 \pm 0.5$ ,  $3 \pm 0.75$ ,  $4 \pm 1$  and  
119  $5 \pm 1.25 \mu\text{m}$ ), then a silicon beam counter ( $55 \pm 5.5 \mu\text{m}$ )[29] and another fixed aluminum degrader  
120 ( $150 \pm 15 \mu\text{m}$ ) as shown in fig. 6. After this, less than 1% of the incoming antiprotons from the  
121 AD are trapped in flight by the Penning trap, while the rest continue downstream.

122 Before entering a six-cross vacuum chamber, where the detector was mounted (fig. 6) the  
123 antiproton beam traversed a  $2 \mu\text{m}$  thick titanium foil used to separate the UHV region from the  
124 secondary vacuum ( $\sim 10^{-7}$  mbar). In the six-way cross the antiprotons were deviated by the  
125 solenoid fringe field before hitting the silicon detector, which was mounted perpendicular to the  
126 beam and 40 mm off axis (fig. 6 and 7).

127 To overcome the unavoidable small inaccuracies in the stopping power calculation through  
128 the degraders' total thickness, the simulation (see sec. 2.2) was independently tuned against the  
129 antiproton trapping efficiency during the tests of the antiproton capture trap. The simulated trapping  
130 efficiency with  $229 \mu\text{m}$  of degrading material was equivalent to the real efficiency obtained with  
131  $225 \mu\text{m}$  of degraders. Nevertheless, the effect of both  $225$  and  $229 \mu\text{m}$  silicon equivalent degrading  
132 material thicknesses were simulated and compared with data presented here for completeness.

133 Fig. 8 shows the kinetic energy distribution of the antiprotons just before reaching the MI-  
134 MOTERA detector as simulated with GEANT4. The average kinetic energy according to simula-  
135 tions was  $\sim 250$  keV for  $225 \mu\text{m}$  material and  $\sim 100$  keV for  $229 \mu\text{m}$ . This energy is higher than  
136 the energy of the antihydrogen in the final system (meV), but much lower than any energy tested to  
137 date. The same simulation shows that  $\sim 60\%$  of the antiprotons coming from the AD reached the  
138 six-way cross chamber. The corresponding distribution of annihilation depths is shown in fig. 9.

139 From the GEANT4 simulations (see sec. 2.2) we could also estimate the spatial distribution  
140 of the antiproton beam. The resulting incident angle of antiprotons on the MIMOTERA was of  
141  $4.5 \pm 1.1^\circ$  with respect to the normal to the detector plane.

142 In order to study the absorption effect on antiprotons and to verify them against the simula-  
143 tions, we covered  $2/3$  of the detector surface with three very thin aluminum foils ( $3$ ,  $6$  and  $9 \mu\text{m}$ ).

144 The foils were suspended parallel to the detector surface at a distance  $\sim 5$  mm by means of three  
 145 thin copper wires with a gauge of  $300 \mu\text{m}$ , also running on the part not covered by the foils.

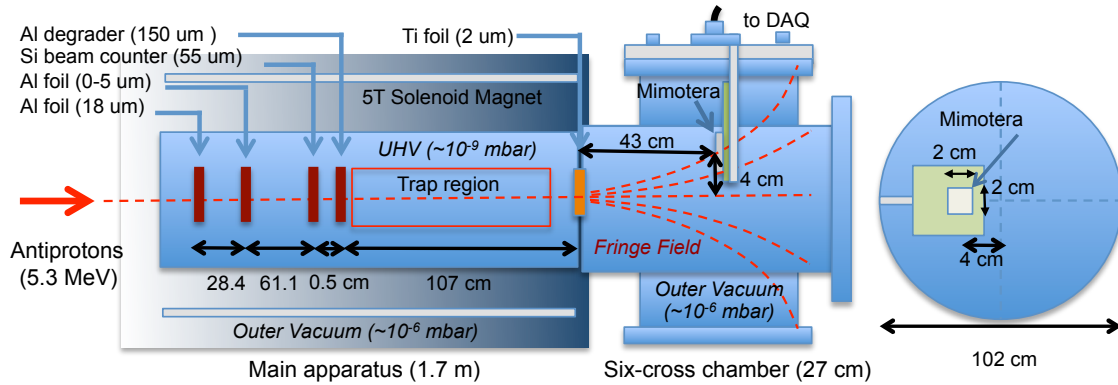


**Figure 6.** Top view (left) and axial view (right) of the test set-up. The center of the silicon detector (MIMOTERA) is installed 40 mm off axis and 430 mm from the main apparatus to avoid saturation due to the high beam intensity.

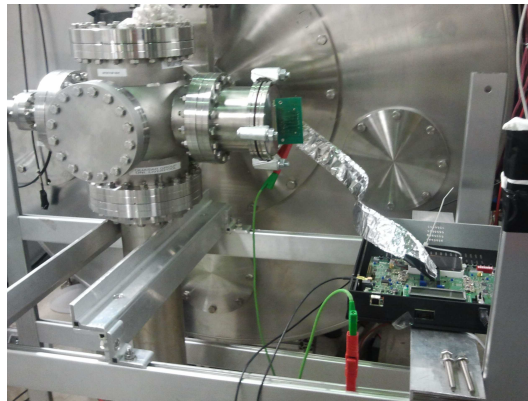


**Figure 7.** Photo of the six-way cross vacuum chamber in testbeam. The MIMOTERA is shown mounted on the right hand flange together with its readout system.

### 146 3.2 The MIMOTERA detector

147 The MIMOTERA [30] is a monolithic active pixel sensor in CMOS technology. It is characterized  
 148 by a large area ( $17 \times 17 \text{ mm}^2$ ), a coarse granularity (with a square pixel of  $153 \mu\text{m}$  size) and a  
 149 dynamic range over 3 orders of magnitude. Moreover, it is back-illuminated, with an entrance  
 150 window  $\sim 100 \text{ nm}$  thick in addition to the  $14 \mu\text{m}$  thick sensitive layer. The detector has a global  
 151 shutter and a continuous read-out with no dead-time: in AEgIS, impinging particles were identified  
 152 by processing the difference between the frame containing the antiproton spill and the previous one  
 153 (differential mode).

154 The MIMOTERA has been designed to be virtually unaffected by cross-talk, in virtue of the  
 155 presence of multiple readout diodes for each pixel. More details can be found in [31, 32].

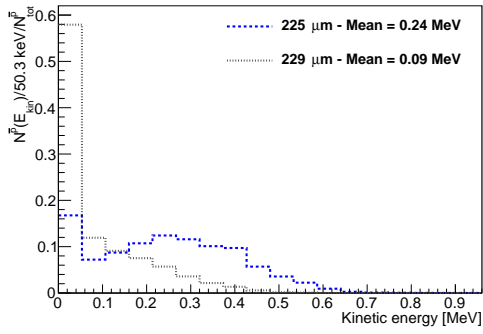


**Figure 8.** Kinetic energy distribution of the antiprotons before they reach the detector, as simulated with GEANT4.

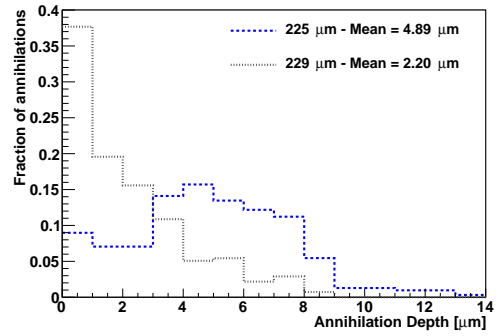


**Figure 9.** GEANT4 simulation showing the annihilation depth, as calculated from the kinetic energy distribution in fig. 8.

156 The full well capacity of the pixels in the MIMOTERA corresponds to a deposited energy of  
 157  $\sim 30$  MeV/pixel.

### 158 3.3 Calibration of the MIMOTERA detector and clustering

159 The MIMOTERA was designed for the profilometry of radiotherapy beams applications for which  
 160 no exact knowledge of the deposited energy is required. Therefore, to determine the amount of  
 161 energy deposited in the detector, the response of the MIMOTERA was calibrated using a red laser  
 162 source ( $\lambda = 660$  nm).

163 The laser light, coming from a custom laser diode assembly at CERN, was directed by means  
 164 of a fiber-coupled focuser onto the aperture window of the detector. A 5 ns pulsed signal was used  
 165 to trigger both the laser diode and the MIMOTERA DAQ, which was operated at 2.5 MHz.

166 To obtain an absolute value for the number of free carriers generated with the laser, the same  
 167 laser was used to induce a transient charge pulse on a PAD diode, 300  $\mu\text{m}$  thick, manufactured by  
 168 HIP (Helsinki Institute for Physics) on Magnetic Czochralski silicon. All the light coming from the  
 169 focuser was projected onto the optical window of the diode, which had the same kind of passivation  
 170 layer as the MIMOTERA (100 nm  $\text{SiO}_2$ ).

171 The signal, decoupled from the DC bias voltage by means of a Picosecond 5531 bias-tee, was  
 172 read and acquired with a 500 MHz LeCroy oscilloscope. The unamplified signal was integrated up  
 173 to  $\sim 100$  ns, where the transfer function of the electronics was measured to be constantly null.

174 Fig. 10 shows the signal distribution in ADC as acquired by the mimotera and a signal transient  
 175 from the diode as induced in both cases by the laser beam.

176 Since the absorption length for 660 nm red light in silicon is  $\sim 3.3$   $\mu\text{m}$  [28], the thickness of  
 177 the active region of the MIMOTERA detector allows to collect more than 98 % of the generated  
 178 charge carriers. As the remaining 2 % could be either reflected or transmitted at the interface  
 179 with the substrate, where the refraction index is unknown, the full 2 % systematic error was added  
 180 to the calibration factor as a conservative estimate. By comparing the analog integrated pulse  
 181 with the pixel charge digitally sampled by the MIMOTERA, we calculate a calibration factor of  
 182  $(4889 \pm 100)$  eV/ADC count. A study verifying the linearity of the MIMOTERA detector can  
 183 already be found in [30].

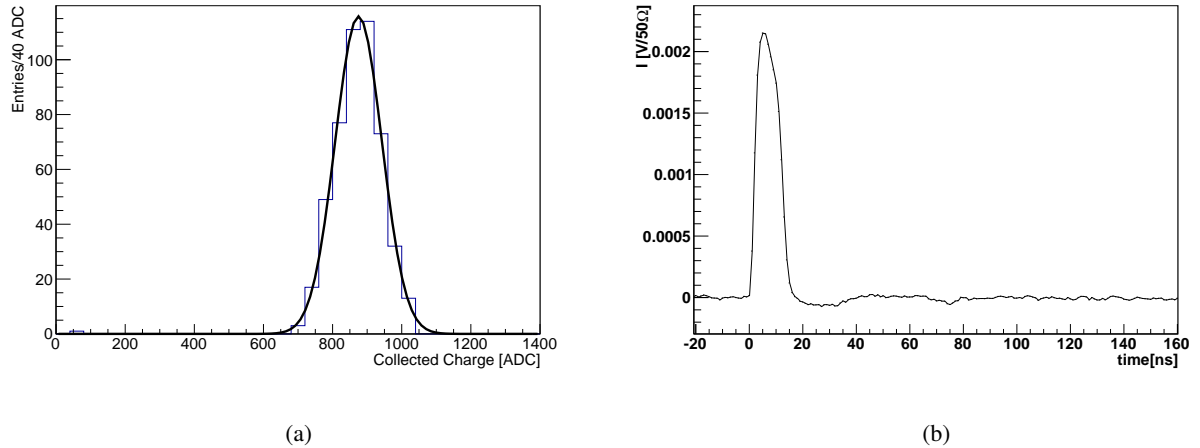


**Figure 10.** Left: distribution of the signal generated by the laser in the MIMOTERA over 491 laser pulses, fitted with a gaussian curve. Right: Transient Current pulse from the HIP diode, as acquired through the oscilloscope, averaged over 1024 pulses.

184 The single pixel noise in the experiment was measured to be 30.3 keV, with fairly low non-  
 185 gaussian tails (fig. 11).

186 The single pixel energy distribution is shown in fig. 12, before and after subtracting the noise  
 187 by fitting a Gaussian to the negative values (where there is no signal). The residual entries with  
 188 energies lower than 5 noise RMS can be attributed to MIP-like pions (depositing between 4.2 keV  
 189 to  $\sim 65$  keV depending on the crossing angle) and protons which for a wide energy range ( $> 50$   
 190 MeV) have a  $dE/dx \simeq 2$  keV/ $\mu\text{m}$ , (see fig. 3). This could possibly explain the peak observed at  $\sim 30$   
 191 keV. More detailed studies in this energy region will be performed in the future beam tests using  
 192 detectors with higher sensitivity to low energies.

193 The complex nature of the annihilation process (see sec. 2.1) was not known and we had no  
 194 estimation on how much of the energy would be deposited away from the annihilation point, for  
 195 instance when a high energy particle creates a long track and deposits its energy in a Bragg peak  
 196 several pixels away. However, having a thin detector would naturally reduce this contribution.

197 We thus developed a clustering routine tailored to our case. Particles impinging or annihilating  
 198 in the MIMOTERA were identified by clusters of neighbouring pixels with a signal exceeding 150  
 199 keV, i.e. 5 standard deviations of the noise distribution. Fig. 13.a shows a raw frame, while fig.  
 200 13.b shows the effect of this cut on the same frame. As part of the validation of the clustering  
 201 algorithm we measured the distance between the center of gravity of each cluster and the pixel  
 202 collecting the highest charge. The results are shown in fig. 14 (for clusters with more than 1 pixel).  
 203 One can see that 97% of the clusters have the highest energy pixel coinciding with the geometrical  
 204 centre. For this reason a seed-driven algorithm using the highest energy pixel of a cluster could  
 205 possibly be used for future analysis of thin detectors.

206 **4. Results**

207 The annihilations produce clusters of fired pixels in different shapes and values of deposited energy,  
208 up to 20 MeV (see fig. 12). As many as 20 pixels can be included in a single cluster and some  
209 annihilations show one or more tracks coming in from the cluster centre in all directions, in a star  
210 shape.

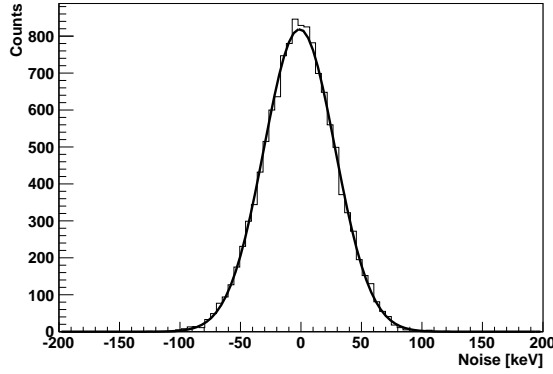


**Figure 11.** Noise spectrum of the MIMOTERA detector for one non-triggered frame.

211 **4.1 Data selection**

212 The efficiency of the clustering algorithm strongly depends on the probability of having two or more  
213 overlapping clusters. For this reason, a veto was applied on frames with too high pixel or cluster  
214 occupancy. Occupancy was varying throughout the data taking because of different configurations  
215 of the focusing magnet. Only frames with a pixel occupancy  $< 10\%$  and less than 150 clusters per  
216 frame were accepted, resulting in  $\sim 25\%$  of the frames being included in the analysis.

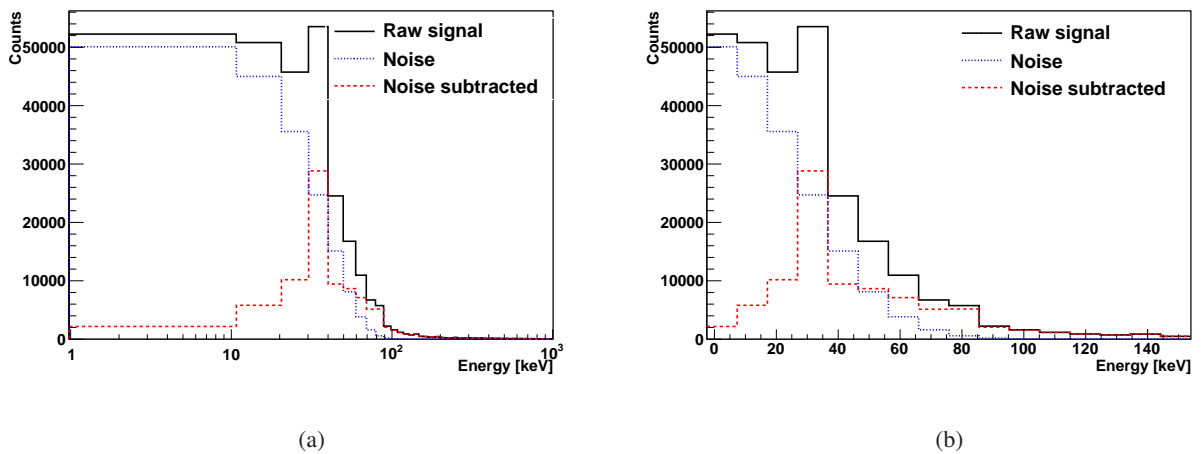


**Figure 12.** Distribution of the signal in single pixels after subtraction of the noise fitted with a normal distribution over the whole range of the acquired data (left) and detail of the low energy region (right).

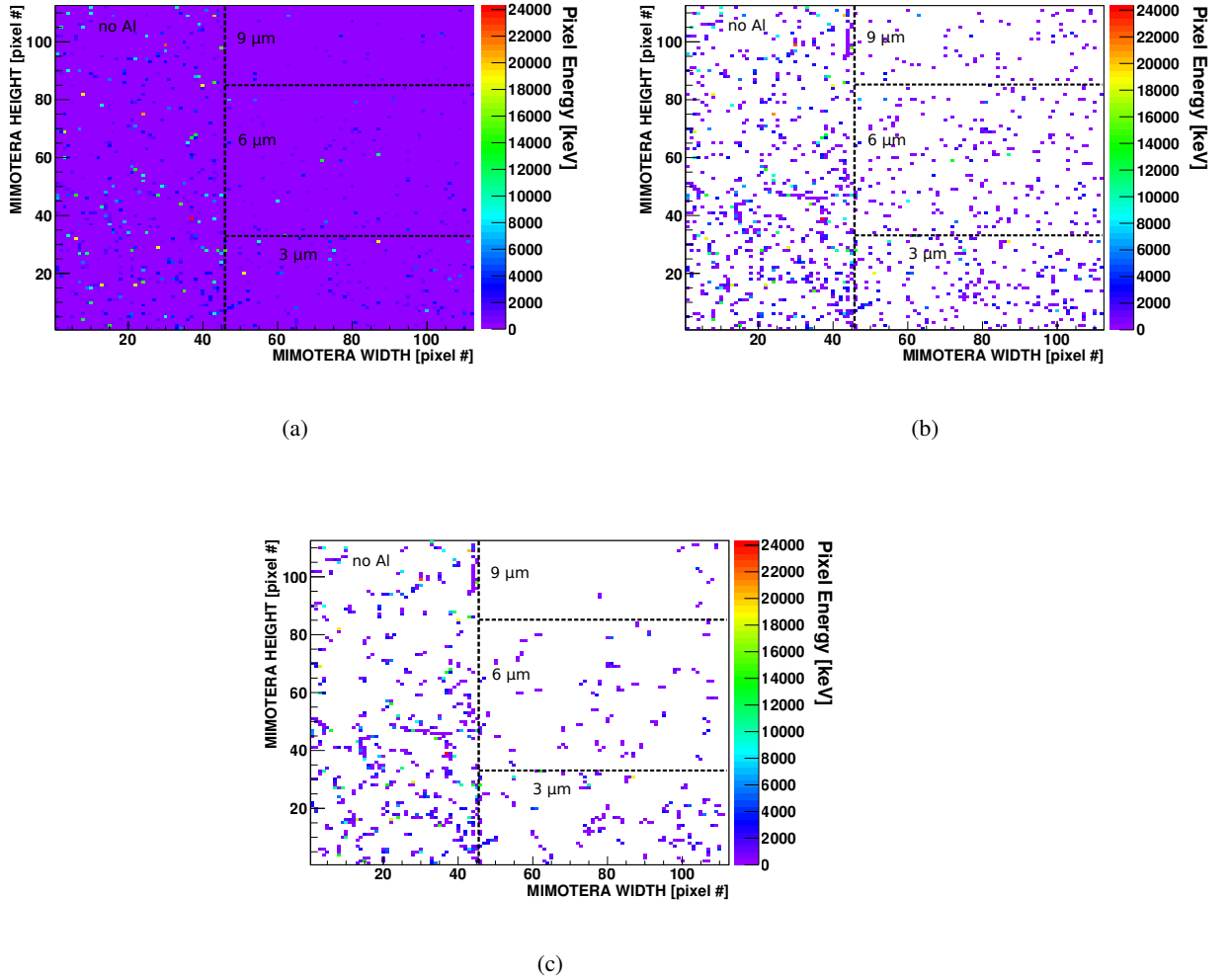


**Figure 13.** Sample of a raw triggered frame (a), after applying the noise cut of 150 keV (b), and with the further exclusion of one-pixel clusters. Around 60% of the detector was covered with different thicknesses of aluminum foil (3, 6, 9  $\mu\text{m}$ ), as shown in the figures.

## 217 4.2 Background sources

218 Two possible background sources were identified as potentially affecting the acquired data. In  
 219 AE $\bar{g}$ IS, heavy ions and protons produced from annihilations in the central region of the apparatus  
 220 are one of the possible background sources. They are expected to arrive quasi-normally on the  
 221 sensor at an angle of  $\sim 0.1$  rad with an estimated 1% probability to produce clusters with a size  
 222 exceeding 1 pixel. It is worth remarking that (see table 2) about one third of the total clusters  
 223 observed were composed by more than one pixel.

224 Two pixels clusters can be generated by a background source only if the source is not quasi-  
 225 normal to the detector itself. The shadow of the wires used to support the Al foils partially masking  
 226 the MIMOTERA was used to estimate the fraction of particles impinging on the detector along  
 227 directions other than normal, most likely due to annihilations in the apparatus. Fig. 16 shows the

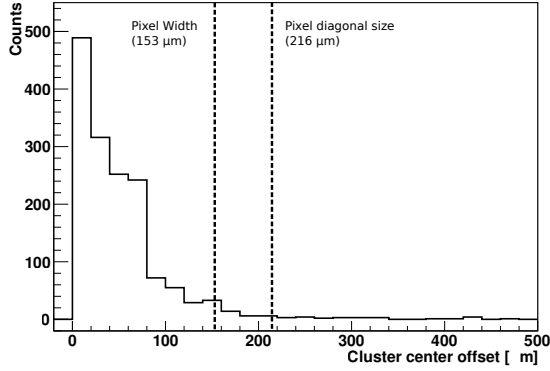


**Figure 14.** Distance offset between the pixel collecting the highest charge in a cluster and the center of gravity of the cluster.

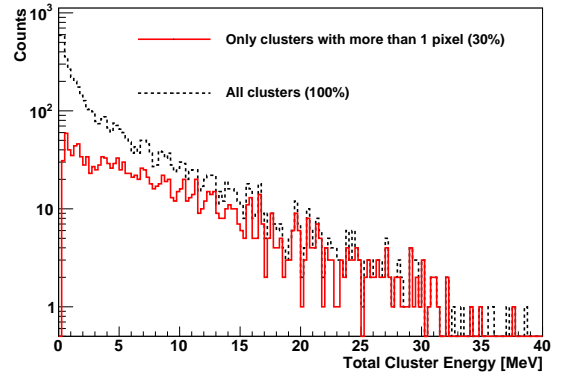


**Figure 15.** Total cluster energy distribution before and after the exclusion of one-pixel clusters (potentially background-affected) from the complete dataset analyzed.

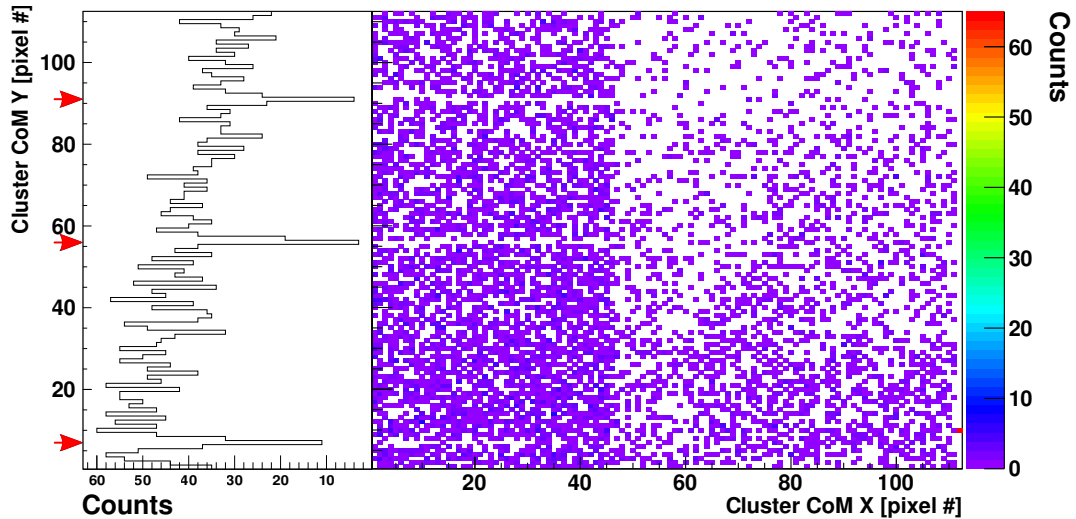


**Figure 16.** Integrated map of cluster center of mass coordinates for the frames used in the analysis, performed for clusters of at least 2 pixels. The red arrows show the location of the supporting wires shadow. Left hand side of the detector was uncovered. The three sections on the right hand side were covered by the 3, 6, 9  $\mu\text{m}$  aluminum foils, bottom to top. The histogram on the left is the projection of the uncovered part, evidencing the shadows of the wires.

228 map of centre of mass (CoM) for all clusters with at least 2 pixels. The shadows left by the wires  
 229 (300  $\mu\text{m}$  gauge) are clearly visible. The wire's geometrical shadow on the sensor can be calculated  
 230 to cover an angle of  $3.5^\circ$ . This angle is quoted with respect to the average direction of the incoming  
 231 antiprotons (see sec. 3.1). Table 2 shows the ratios between the number of clusters in shadowed  
 232 and unshadowed rows for different cluster sizes. While the contamination for single pixel clusters  
 233 is at the 16.0% level, it drops to the 7% level for larger clusters.

234 These numbers set a limit for the purity of the sample by particles travelling with high di-



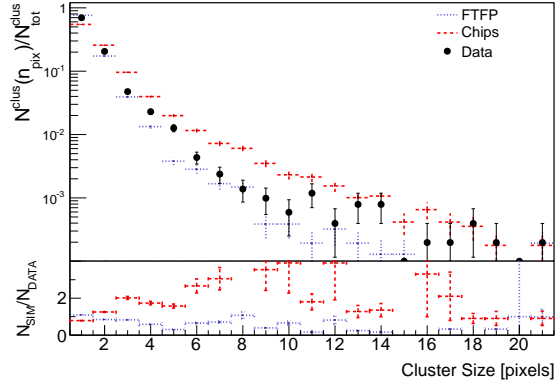


**Figure 17.** Cluster size distribution for data and the two studied simulation models. Most clusters have 1 or 2 pixels, but some clusters consist of as many as 20 pixels.

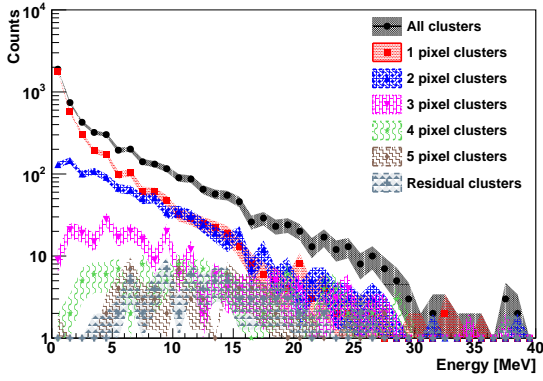


**Figure 18.** Cluster energy spectrum for different cluster sizes showing a large spectrum for all sizes up to 40 MeV. Clusters with few pixels mostly have low energy, while as the clusters get larger they are more evenly distributed.

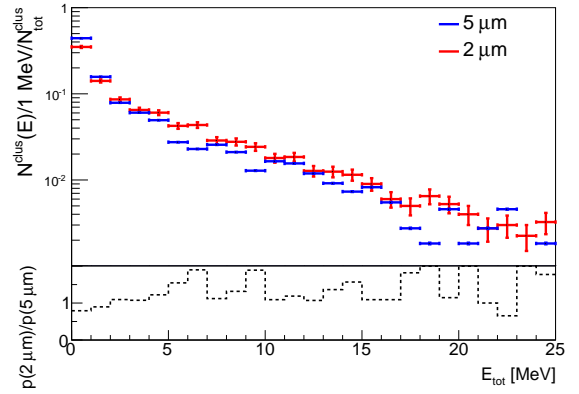


**Figure 19.** Total energy for clusters produced by antiprotons passing through 2  $\mu\text{m}$  and 5  $\mu\text{m}$  thick mobile degrader.

Min. Clus. Size (pix.)	N. of clusters	Cluster ratio in shadowed area (%)
1	11 537	16.0 $\pm$ 3.4
2	4 401	7.4 $\pm$ 3.6
3	1 911	9.3 $\pm$ 6.4
4	1 056	8.2 $\pm$ 7.7

**Table 2.** Fraction of clusters centers of mass in rows shadowed by wires with respect to clusters in neighboring rows, for the region not covered by Al foils.

235 divergence from the antiproton flux. This contrast ratio also represents the contamination limit for  
 236 particles different from antiprotons. Any further cut on the number of pixels doesn't introduce any

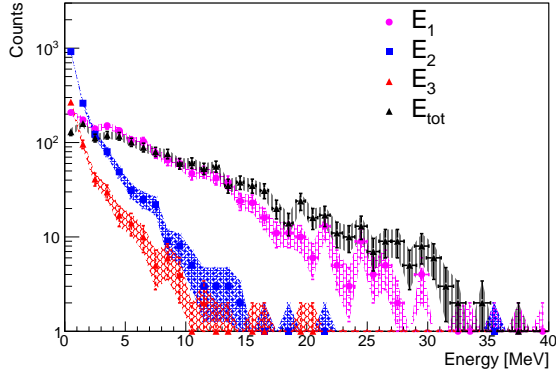


**Figure 20.** Energy distributions for  $E_1$ ,  $E_2$ ,  $E_3$ ,  $E_{tot}$  (with  $E_1$  energy of the pixel with highest energy in a cluster,  $E_2$  energy of the pixel with the second highest energy,  $E_3$  the sum of all residual pixels and  $E_{tot}$  total cluster energy) for clusters with more than one pixel.

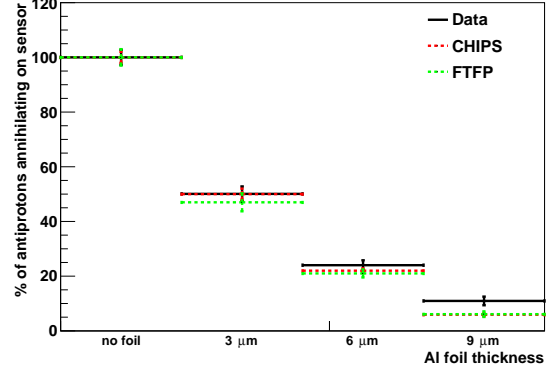


**Figure 21.** Fraction of annihilations on the sensor parts covered with different thicknesses of Al foil. This analysis is performed only with clusters consisting of more than 3 pixels.

237 significant improvement, while reducing the statistics. Fig. 13.c shows a sample frame after the  
 238 cut on single pixel clusters, and fig. 15 shows the effect of this cut on the cluster energy distribution.

239 For the reasons exposed above, a more detailed analysis on the energy and size of the clusters  
 240 and comparison with simulations will only be shown for the sample with highest purity, i.e. the  
 241 one composed by clusters with at least two pixels.

### 242 4.3 Cluster characteristics

243 Fig. 17 shows the distribution of cluster sizes for both data and the two simulation models. Al-  
 244 though we find clusters as big as 20 pixels,  $\sim 2/3$  of the events are formed by one pixel and  $\sim 1/3$   
 245 of two or more pixels, indicating a prevalence of localized energy deposits.

246 The total cluster energy spectrum is seen in fig. 18, showing cluster energies as large as 40  
 247 MeV. This figure also shows the energy distribution of clusters of different sizes, and one can see  
 248 that the energies of a given cluster size are distributed over the entire energy range. Small clusters  
 249 are most often produced at low energies, with a sloped distribution decreasing towards higher  
 250 energies. As the size of the clusters increases, the slope of the energy distribution flattens out and  
 251 the minimum energy is shifted upwards, starting above  $\sim 1$  MeV for clusters with 4 pixels or more.

252 Since data were taken with two different degrader configurations, the datasets were studied  
 253 in order to verify whether there was enough statistically significant difference to justify a separate  
 254 analysis. We separated the events collected with 2 and 5  $\mu\text{m}$  degrader, and the corresponding en-  
 255 ergy spectrum can be seen in fig. 19. The overall distribution of the energy of the annihilation  
 256 clusters is very similar for both degraders. Small statistically significant differences can be ob-  
 257 served for only a few bins, probably related to the differences in the penetration depth (and hence  
 258 the deposited kinetic energy) in silicon for the two degraders configuration. However, given the non  
 259 systematicity of the difference, we decided to consider the two datasets together, thus improving  
 260 significantly the statistics.

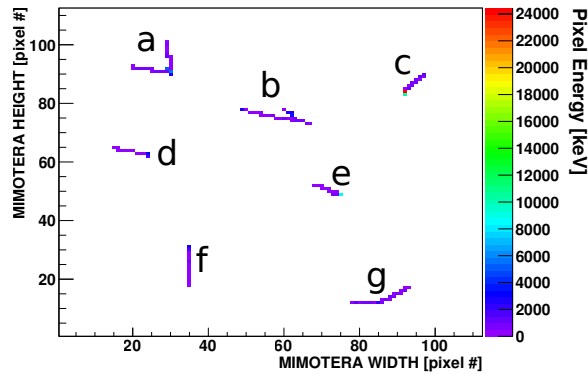


**Figure 22.** Sample of in-plane tracks observed with the MIMOTERA detector. A description of the tracks is provided in table 3.

261 Fig. 20 shows how the energy is distributed among the pixels composing the clusters.  $E_1$  is  
 262 the energy distribution of the pixel with the highest energy in the cluster,  $E_2$  the pixel with the  
 263 second highest energy,  $E_3$  the residual energy and  $E_{tot}$  the total cluster energy. These distributions  
 264 are shown after cutting on 1 pixel clusters. For all clusters, most of the energy is concentrated in  
 265 one single pixel.

266 The additional Al foils covering the detector were used to study the energy loss of antiprotons  
 267 in silicon. To be sure to study antiprotons which annihilated inside the silicon, we counted clusters  
 268 with more than 3 pixels only. This cut removes not only single pixel clusters from particles annihi-  
 269 lating in the foils or elsewhere in the apparatus but also excludes the rare case where a secondary  
 270 particle passes at the intersection of 2 pixels. Since we have shown that data taken with the two  
 271 degraders were compatible (fig. 19), the results which include the additional Al foil are shown in  
 272 fig. 21 for both types of degraders – 2 and 5  $\mu\text{m}$ . About  $\sim 10\%$  of the antiprotons were able to  
 273 pass through the 9  $\mu\text{m}$  aluminum foil. The results for the different aluminum thicknesses are in  
 274 agreement with both simulation models, showing that the models provide a good description of the  
 275 stopping power of antiprotons in matter.

#### 276 4.4 Tracks recognition

277 Measuring track lengths and  $dE/dx$  proved to be a useful method to identify some of the anni-  
 278 hilation products travelling in the silicon detector. Given the small thickness of the MIMOTERA  
 279 active region, products traveling in the detector plane were scarce. However, we were still able to  
 280 distinguish 21 clusters having one, two or three ion tracks.

281 To identify the annihilation products we calculated the ranges and  $dE/dx$  for the most impor-  
 282 tant ion species produced in the annihilation process [25]. As mentioned in sec. 2.2, fig. 3 shows  
 283 the deposited energies and fig. 4 shows the corresponding ranges. For heavy ion species with low  
 284 energies, where the range is  $< 14 \mu\text{m}$ , the total particle kinetic energy is expected to be deposited  
 285 in the detector.

286 Fig. 22 shows examples of typical clusters with tracks, and table 3 lists the properties of all  
 287 tracks found. From the deposited energy most of the tracks can be identified as protons, while one

288 track probably originates from a heavier ion.

N. of prongs	Seed energy (MeV)	Prongs length ( $\mu\text{m}$ )	Prongs $dE/dx$ (keV/ $\mu\text{m}$ )	Identification
1	none	1630	1.18	Proton $> 100$ MeV
1	9.9	2950	2.11	Proton $\simeq 50$ MeV
(d)1	4.9	1650	1.63	Proton $\simeq 70$ MeV
(c)1	34.8	1080	6.66	Proton $\simeq 10$ MeV
1	2.6	1840	2.73	Proton $\simeq 40$ MeV
1	17.6	2170	7.06	Proton $\simeq 10$ MeV
(f)1	4.4	1840	2.44	Proton $\simeq 40$ MeV
1	8.8	2300	1.34	Proton $\simeq 100$ MeV
1	none	1740	2.16	Proton $\simeq 50$ MeV
1	none	7220	1.12	Proton $> 100$ MeV
1	12.1	2170	2.8	Proton $\simeq 30$ MeV
1	8.6	1730	2.1	Proton $\simeq 50$ MeV
1	6.9	1780	1.2	Proton $> 100$ MeV
1	2.3	2380	2.8	Proton $\simeq 40$ MeV
1	11.1	2190	3.4	Proton $\simeq 30$ MeV
1	none	2900	3.1	Proton $\simeq 30$ MeV
(e)1	none	1220	3.0	Proton $\simeq 30$ MeV
(g)2	2.2	1100, 1500	3.9, 3.27	Protons $\simeq 30$ MeV
2	11.1	340, 2080	0.7, 1.2	Protons $> 100$ MeV
(a)2	13.5	1510, 1620	4.0, 2.4	Protons $\simeq 20, 50$ MeV
(b)3	none	2200, 900, 750	2.4, 4.1, 15	Prot. (50, 20 MeV) + Heavy Ion

**Table 3.** Clusters which are identified as having one or more tracks. Clusters marked with a letter are shown in fig. 22. Seeds are here defined as pixels located at one end of the track(s) with pixel energy in excess of 1 MeV.

#### 289 4.5 Comparison with Monte Carlo simulations

290 The Monte Carlo samples were generated separately for CHIPS and FTFP and consist of 3 million  
 291 events each. The entire flight path of the antiprotons was simulated, starting with the 5.3 MeV  
 292 antiprotons from the AD, including all of the AEGIS apparatus (full geometry and 5 T magnetic  
 293 field), ending with the annihilations on the silicon detector. In the nominal case, with 225  $\mu\text{m}$  total  
 294 degrader thickness, only  $\sim 25\,000$  antiprotons of the original 3 million annihilated on the detector  
 295 according to the simulations. For 229  $\mu\text{m}$  thickness this number decreased to  $\sim 20\,000$ .

296 Fig. 23 and 24 show the total energy distribution and the particle composition of clusters  
 297 for the two simulation models. For CHIPS one expects higher cluster energies and a broader  
 298 distribution containing more alpha particles and protons and less heavy nuclei than for FTFP.

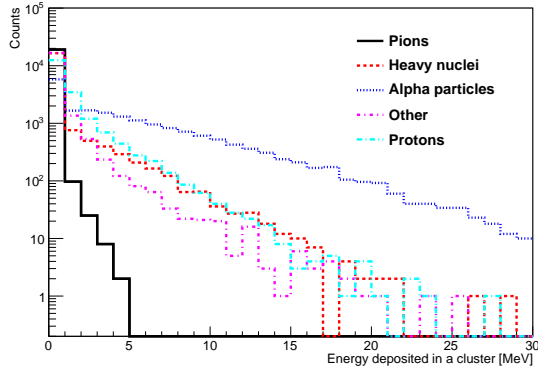


**Figure 23.** Fraction of cluster energy for different annihilation products, as simulated with CHIPS.

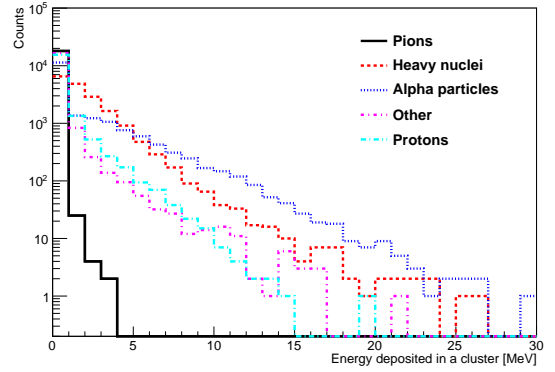


**Figure 24.** Fraction of cluster energy for different annihilation products, as simulated with FTFP.

299 The signal in single pixels was obtained from the ionizing energy deposited by particles in the  
 300 geometrical volume covered by the pixel cell.

301 The clustering algorithm developed for the data analysis was also implemented in the simula-  
 302 tions. Random gaussian noise was included as well, with the same RMS obtained from the data.  
 303 As simulations of antiproton annihilations have not yet been validated at low energies, we present  
 304 a comparison between data and simulations for an energy range of 0-25 MeV of energy released in  
 305 the detector. Fig. 25 shows a comparison between data and simulation for the total cluster energy  
 306 for clusters composed by more than one pixel. Agreement is generally poor with both simulation  
 307 models up to energies of 5 MeV. At energies above 5 MeV, FTFP shows a better agreement to data.

308 Fig. 26 shows the energy distribution of the highest energy pixel in the clusters for clusters with  
 309 more than one pixel. When compared with fig. 25, we see that the total cluster energy distribution  
 310 is dominated by the contribution of the highest energy pixel. Also in this case the agreement with  
 311 CHIPS and FTFP is poor < 5 MeV and improve significantly above this energy for the FTFP  
 312 model. The same validation was made for the quantities  $E_2/E_{tot}$  and  $E_3/E_{tot}$ , showing in this case  
 313 agreement within statistical errors between data and simulations for both models.

314 To verify the reliability of the simulations and its dependence on the chosen threshold cut, a  
 315 scan was performed in the range of 100-600 keV for the same parameters discussed above. The  
 316 cluster size distribution in fig. 27 shows a good description of data points with the FTFP model  
 317 (with a slight underestimation), while CHIPS systematically overestimates the cluster size to a  
 318 maximum of  $\sim 30\%$  at lower cut energies. The relative neutrality of the FTFP is explained with  
 319 the smaller overall cluster size that the model provides and considering that all the curves tend to  
 320 the same asymptotic value (2).

321 The  $E_1/E_{tot}$  distribution, with the exclusion of 1 pixel clusters, shows a good agreement be-  
 322 tween data and FTFP simulations (fig. 28). The observed overall negative slope has to be explained  
 323 with a flattening of the clusters with the increasing cut: clusters having low-energy pixels will be  
 324 excluded from the statistics. The decreasing  $E_1/E$  ratio indicates that the highest pixel energy is  
 325 not strictly correlated to the total cluster energy.

326 Good agreement was also found for  $E_2/E_{tot}$  and  $E_3/E_{tot}$  for both simulation models. In the

327 case of FTFP, the mean cluster size remains essentially unchanged by the pixel noise cut, while the  
 328  $E_1/E_{tot}$  ratio shows a strong dependence on the noise cut.

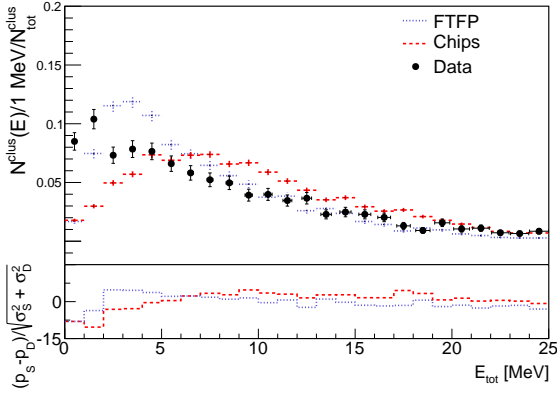


**Figure 25.** Distribution of the total cluster energy, excluding the one-pixel clusters.

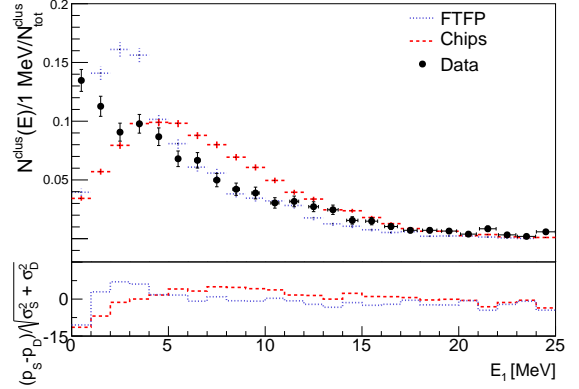


**Figure 26.** Distribution of the energy deposited only in the pixel collecting the highest charge for each cluster, excluding the one-pixel clusters.

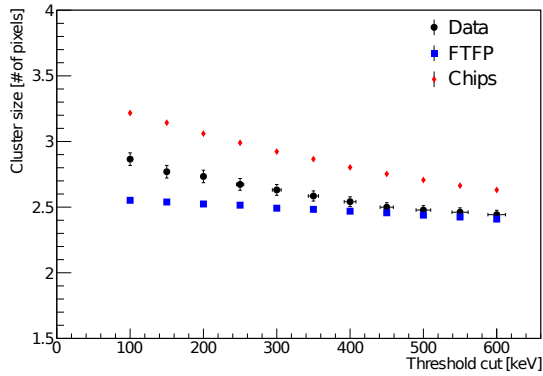


**Figure 27.** Mean cluster size versus the noise cut, excluding the one-pixel clusters.

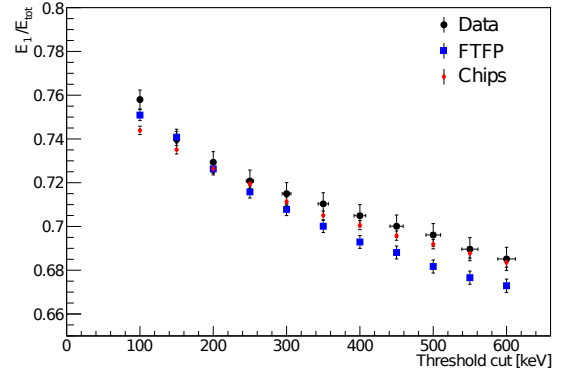


**Figure 28.**  $E_1/E_{tot}$  - the amount of energy deposited only in the highest energy pixel in the cluster vs the noise cut, excluding the one-pixel clusters.

## 329 5. Summary and Conclusions

330 We have successfully measured the first on-sensor annihilations of antiprotons in silicon using a  
 331 pixelated silicon imaging detector: an important milestone and the first step on the way to designing  
 332 a novel position sensitive detector for measuring the gravitational effect on antihydrogen. We also  
 333 performed the first validation of GEANT4 for low energy antiprotons. The main results are as  
 334 follows:

- 335 • Study of clusters from antiproton annihilations measuring:
  - 336 – Cluster sizes ranging between 1 and 20 pixels, with a mean value of  $2.77 \pm 0.048$  with
  - 337 the MIMOTERA pixel size ( $153 \times 153 \mu\text{m}^2$ ,  $14 \mu\text{m}$  thickness.)

- 338           – Cluster energies up to 40 MeV.
- 339           – Measurement of prongs up to 2.9 mm.
- 340           – Discrimination and identification of annihilation products such as protons and heavy
- 341           ions.
  
- 342       • Study of the energy loss of antiprotons in aluminum, validating the simulation with 10%
- 343       maximum deviation from experimental data.
  
- 344       • Comparison of two GEANT4 simulation models for low energy antiprotons, CHIPS and
- 345       FTFP, showing a generally poor agreement for both models at energies  $<5$  MeV while FTFP
- 346       provides a better description of data points for energies  $>5$  MeV: while the results are not
- 347       statistically compatible, the simulation are still providing a reasonable description of the
- 348       event, especially at higher energies.

349       These results will allow to identify methods to determine the annihilation position, both by  
350       position extrapolation from proton tracks and center of mass methods. It will also be the basis for  
351       simulations and design of the first prototype antihydrogen silicon detector for AEGIS.

## 352   **Acknowledgments**

353       We would like to thank the Research Council of Norway and the Bergen Research Foundation  
354       for their support. We would like to thank the CERN SSD lab, especially in the persons of Michael  
355       Moll and Maurice Glaser, for having provided the instrumentation and infrastructures used for laser  
356       calibration measurements. We would also like to thank Alberto Ribon for his help with the fine  
357       tuning of GEANT4 with antiprotons as well as with the interpretation of the results.

358 **References**

- 359 [1] The AEGIS collaboration - *Proposal for the AEGIS experiment at the CERN antiproton decelerator*  
360 2007
- 361 [2] Los Alamos Report LA-UR 86-260
- 362 [3] M. Nieto and T. Goldman *The arguments against antigravity and the gravitational acceleration of*  
363 *antimatter* Physics Reports, vol 205, issue 5, 1991 (221)
- 364 [4] T. Brando et al. *Observations of low-energy antineutrons in a time-separated neutral beam* Nuclear  
365 *Instruments and Methods*, vol 180, issues 2-3, 1981 (461)
- 366 [5] M. Longo et al. *New Precision Tests of the Einstein Equivalence Principle from SN1987A* - Physical  
367 *Review Letters*, vol 60, no. 3, 1988 (173)
- 368 [6] A. P. Mills Jr. and M. Leventhal *Can we measure the gravitational free fall of cold Rydberg state*  
369 *positronium?* Nuclear Instruments and Methods in Phys. Res. B, vol 192, Issues 1-2, 2002 (102)
- 370 [7] The ALPHA Collaboration and A.E. Charman *Description and first application of a new technique to*  
371 *measure the gravitational mass of antihydrogen* - Nature Communications, DOI: 10.1038/ncomms2787
- 372 [8] *The GBAR experiment: gravitational behaviour of antihydrogen at rest* Class. Quantum Grav. 29  
373 184008, 2012
- 374 [9] M. Doser et al. - *Exploring the WEP with a pulsed cold beam of antihydrogen* Class. Quantum Grav. 29  
375 184009
- 376 [10] G. Testera et al. *Formation of a cold antihydrogen beam in AEGIS for gravity measurements* AIP  
377 *Conference Proceedings* 1037, 5, 2008
- 378 [11] Markus K. Oberthaler et al. *Inertial sensing with classical atomic beams* Physical Review A, vol 54,  
379 1996 (3165-3176)
- 380 [12] C. Amsler et al. *A new application of emulsions to measure the gravitational force on antihydrogen*  
381 *Journal of Instrumentation*, vol 8, 2013 P02015
- 382 [13] S. Aghion et al. *Prospects for measuring the gravitational free-fall of antihydrogen with emulsion*  
383 *detectors* Journal of Instrumentation, vol 8, 2013 P08013
- 384 [14] McGaughey et al. *Low energy antiproton-nucleus annihilation radius selection using an active silicon*  
385 *detector / target* Nuclear Instruments and Methods, vol 249, 1986 (361-365)
- 386 [15] Bendiscioli G., Kharzeev D. *Antinucleon-Nucleon and Antinucleon-Nucleus Interaction. A Review of*  
387 *Experimental Data* - Rivista del Nuovo Cimento vol. 17, n. 6
- 388 [16] R.Medenwaldt et al. *Measurement of the stopping power of silicon for antiprotons between 0.2 and 3*  
389 *MeV* Nuclear Instruments and Methods in Phys. Res. B, vol 58, 2002 (1)
- 390 [17] The ATHENA collaboration *The ATHENA antihydrogen apparatus* - Nuclear Instruments and  
391 *Methods in Physics Research A*, vol. 518, 2004 (679-711)
- 392 [18] H. Spieler *Semiconductor Detector Systems* - Oxford University Press, 2005
- 393 [19] The ASTERIX collaboration *Search for monochromatic pion emission in  $p\bar{p}$  annihilation from atomic*  
394 *p states* Physics Letters B, vol 152, 1985 (135)
- 395 [20] J.F. Ziegler et al. *SRIM - The Stopping and Range of Ions in Matter* Lulu Press



- 396 [21] I. Hrivnacova et al. The Virtual Monte Carlo - Computing in High Energy and Nuclear Physics, La  
397 Jolla, March 24-28, 2003
- 398 [22] P. V. Degtyarenko, M. V. Kossov, and H.P. Wellisch - *Chiral invariant phase space event generator, I.*  
399 *Nucleon-antinucleon annihilation at rest* - Eur. Phys. J. A 8, 217-222 (2000)
- 400 [23] A. Galoyan, V. Uzhinsky *Simulation of Light Antinucleus-Nucleus Interactions* arXiv:1208.3614
- 401 [24] Geant4 Physics Reference Manual
- 402 [25] W. Markiel et al. *Emission of Helium ions after antiproton annihilation in nuclei* - Nuclear Physics A,  
403 vol 485, 1988 (445-460)
- 404 [26] D. Bassignana et al. *First investigation of a novel 2D position-sensitive semiconductor detector*  
405 *concept* - Journal of Instrumentation (2012) JINST 7 P02005
- 406 [27] C. Regenfus *A cryogenic silicon micro-strip and pure-CsI detector for detection of antihydrogen*  
407 *annihilations* - Nuclear Instruments and Methods in Physics Research A 501, 2003, p. 65
- 408 [28] Edward D. Palik, Handbook of Optical Constants of Solid (1985), Academic Press, NY.
- 409 [29] P. Riedler et al. *Performance of ultra-thin silicon detectors in a 5 MeV antiproton beam* - Nuclear  
410 Instruments and Methods in Physics Research A 478, 2002, p.316
- 411 [30] R. Boll et al. *Using Monolithic Active Pixel Sensors for fast monitoring of therapeutic hadron beams* -  
412 *Radiation Measurements* vol. 46, Issue 12, 2011 (1971-1973)
- 413 [31] L. Badano *Développement d'un moniteur de faisceau innovant pour la mesure en temps réel des*  
414 *faisceaux utilisés en hadronthérapie* - Université Louis Pasteur Strasbourg I (2005)
- 415 [32] R. Boll Diploma thesis - University of Heidelberg (2010)